Measurement 152 (2020) 107328

Contents lists available at ScienceDirect

Measurement

journal homepage: www.elsevier.com/locate/measurement

Design and optimization of a high sensitivity joint torque sensor for robot fingers

Kang Han [a,b], Liheng Chen [a,b,*], Mingyi Xia [a], Qinwen Wu [a,b], Zhenbang Xu [a,b], Guoqiang Wang [c]

[a] Innovation Lab of Space Robot System, Space Robotics Engineering Center, Changchun, Institute of Optics, Fine Mechanics and Physics, Chinese Academy of Sciences, Changchun, 130033, China
[b] University of Chinese Academy of Sciences, Beijing, 100049, China
[c] College of Mechanical Science and Engineering, Jilin University, Changchun, 130012, China

ARTICLE INFO

Article history:
Received 10 August 2019
Received in revised form 15 October 2019
Accepted 25 November 2019
Available online 29 November 2019

Keywords:
Finger joint torque sensor
Three-fingered dexterous hands
Optimal design
Response surface methodology
Sensitivity

ABSTRACT

In order to protect target objects from being destroyed, the torque exerted on finger joints should be accurately measured and used for controlling the dexterous robotic hand. However, restricted by the space of the finger joint, it is difficult to improve the sensitivity of the finger joint torque sensors. To solve this problem, a novel joint torque sensor with floating beams and supporting beams is designed based on an analysis of the traditional cross-beam torque sensor. The structure of the sensor is newly modeled and analyzed. Then response surface methodology (RSM) is employed to optimize the sensor structural parameters. A comparison of finite element analysis results and optimization results is used to estimate the sensitivity of the proposed sensor and verify the optimized attachment positions for the strain gauges. Finally, a finer joint torque sensor is fabricated and calibrated. The results show a good performance of repeatability, nonlinearity, hysteresis and sensitivity.

1. Introduction

The development of three- and five-fingered dexterous robotics hands has become a focus in robotics research [1,2]. A dexterous hand can perform multiple operations and complex movements. To determine the characteristics of the manipulated object, it is necessary to install a variety of sensors in a dexterous hand, including tactile sensors and force sensors. Finger joint torque sensors measure the moment of each joint in the dexterous hand and feed it back to the control system. Ideally, the control system should determine the force exerted on the target object by the dexterous hand to prevent the target object from being destroyed or slipping out during the grasping process [3–5]. A joint torque sensor with a higher sensitivity can obtain more physical information about the target object, which assists target recognition [6]. Because of the limited space available for a dexterous finger joint, improving the sensitivity of a finger joint torque sensor is very difficult [7–8]. To achieve high sensitivity, the structure and parameters of the sensor must be optimized.

Previous studies on torque sensors are mainly based on strain gauges. Pérez R U et al designed an ultra-low-cost torque sensor with crossbeams, which improved the sensitivity of the torque sensor by drilling around strain beams and reducing the width of strain beams [9]. Sun Y developed a six-axis force/torque sensor for the Chinese space robot, and employed RMS to get the optimum parameters. They designed through-holes on the cross beam to improve the sensitivity of the sensor [10]. Zhang HX et al developed a torque sensor using a 4-bar linkage shape to improve the sensitivity [11]. But the diameter of the sensor is Φ150 mm. Yuan C et al proposed a multi-axis force/torque sensor composed of two connected cross-beams [12]. The size of the sensor is Φ50 mm × 12 mm and the sensor sensitivity is 813.6 μV/Nm, which can be used in robot feet. Liang Q et al presented a 4-D fingertip force sensor based on an E-type membrane elastomer and strain gauges [13–14], which can measure the force F_x, F_y, F_z and M_z. It is 30 mm in diameter and 35 mm in length with a good performance in linearity. Besides, there are also other types of torque sensors or multi-axis force/torque sensors to realize the measurement of the moment acted on joints [15–17]. However, the size of usual torque sensors is not suitable for robot finger joints. ATI industrial automation designed a series of commercial off-the-shelf six-axis sensors [18]. The size of the smallest one (Nano 17) is Φ17 mm × 14 mm. But commercial torque sensors are expensive, and specifications are inappropriate for finger joint application.

Moreover, a variety of researchers developed miniaturized torque sensors based on other measurement principles. Melchiorri C

* Corresponding author.
E-mail address: chenliheng3@163.com (L. Chen).

https://doi.org/10.1016/j.measurement.2019.107328
0263-2241/

et al presented a novel force/torque sensor based on optoelectronic components [19], which can be used in the finger of robotic hands, but its error increases with the frequency of the input signal. Kaneko M et al proposed a tension differential type torque sensor for a finger actuation with tendons [20], which has a single body compared with the conventional approach. However, it is only suitable for particular finger joints. Lee D H et al presented a capacitive-type six-axis force/torque sensor for robotic application [21]. The size of the sensor is Φ25 mm × 19 mm. Based on simply-supported beam and optoelectronics, Noh Y et al presented a multi-axis force/torque sensor used for a continuum robot [22]. The size of the sensor is Φ24 mm × 12 mm. Jung K et al developed a fingertip sensor based on the semiconductor strain-gage. It has a size of Φ26 mm × 18 mm and the accuracy of the sensor is 6% [23]. Hwang Y et al proposed a virtual torque sensor for commercial RC servo motors based on dynamic system identification utilizing parametric constraints [24], which can be used for robot finger equipped with RC servo motors without the physical torque sensor. However, the measurement is not precise enough, only fit for prototype robots. Although there are many of toque sensors based on different principles, they are not mature enough in measurement properties or environmental adaptability.

In recent years, research on torque sensors has mainly focused on miniaturization and structural integration. Kim T K et al. integrated a torque sensor into a robot finger frame, and calibrated the sensor after assembling the finger [25]. Jung B J et al. attached strain gauges to a flexible wheel with split harmonic deceleration to measure the joint moment [26]; their design reduced both the required space and cost. However, because the flexible wheel deforms during the operation of the harmonic decelerator, the measured data must be filtered, reducing the measurement accuracy. Mouri T et al. designed a space-efficient torque sensor based on the tensile and compressive strains on a motor mounting seat [27], which used the space efficiently. Kim D H et al. designed two types of moment sensor, namely one- and two-axis torque sensors, to measure the moment of a finger joint and the joint between a finger and the palm, respectively [28]. The one-axis force sensor adopted a conventional four-beam structure, and the two-axis torque sensor adopted a bending beam structure.

Most finger joint torque sensor designs focus on miniaturization. Performance optimization of miniature torque sensors is seldom conducted. In this paper, we increase the measurement accuracy of a finger joint torque sensor by improving the structure of the sensor after a detailed analysis of the measurement principle of a conventional joint torque sensor. Response surface methodology (RSM) is used to determine the optimal structural parameters for the sensor. The purpose of this work is not only to design a torque sensor for a dexterous hand, but also to find a way to optimize a torque sensor based on the strain gauge.

2. Structural design of the finger joint torque sensor

2.1. Three-fingered dexterous hand

The proposed finger joint torque sensors were installed on a three-fingered dexterous hand. The hand was composed of a bottom base and three fingers, as shown in Fig. 1. The total length of the hand was 229 mm, and the length of each finger was 142 mm. Each finger had two finger joints driven by a DC motor and a harmonic reducer, which were connected by a synchronous belt. The output torque of each finger joint was 2 N·m. The torque sensors were installed at the output position of the harmonic reducer. The driving torque of each joint was output through the torque sensor, to ensure that the torque sensor measured all the torque for the finger joint. A magnetic coder, which fed the rotation angle of the joint back to the control system, was installed on the other side of the joint. To match the size requirements for the finger joint, the outer diameter of the torque sensor was less than 31 mm, and the central block that was connected to the harmonic reducer was larger than the harmonic reducer output axis. The measurement range of the torque sensor had to meet the maximum grip force requirement of the dexterous hand.

2.2. Measurement principle of the torque sensor

The design of the elastomer plays a critical role in a torque sensor based on the strain gauge [10]. The structure of a conventional elastomer is shown in Fig. 2. The main components are a rim ring B, four strain beams L1–L4 and a central block O. The strain-type elastomer used in the torque sensor usually has a symmetrical structure to ensure measurement linearity. Four strain gauges are bonded to both sides of the two symmetrically distributed strain beams to form the full-bridge circuit shown in Fig. 3. When the sensor is working, the rim ring is fixed and load torque is applied to the central block. The tensile or compressive strains on the strain beams are measured by the strain gauges and used to calculate the load torque.

The output voltage of the full bridge circuit is expressed as:

$$V_{out} = \left(\frac{R_4 + \Delta R_4}{R_1 - \Delta R_1 + R_4 + \Delta R_4} - \frac{R_3 - \Delta R_3}{R_2 + \Delta R_2 + R_3 - \Delta R_3}\right) V_{in} \quad (1)$$

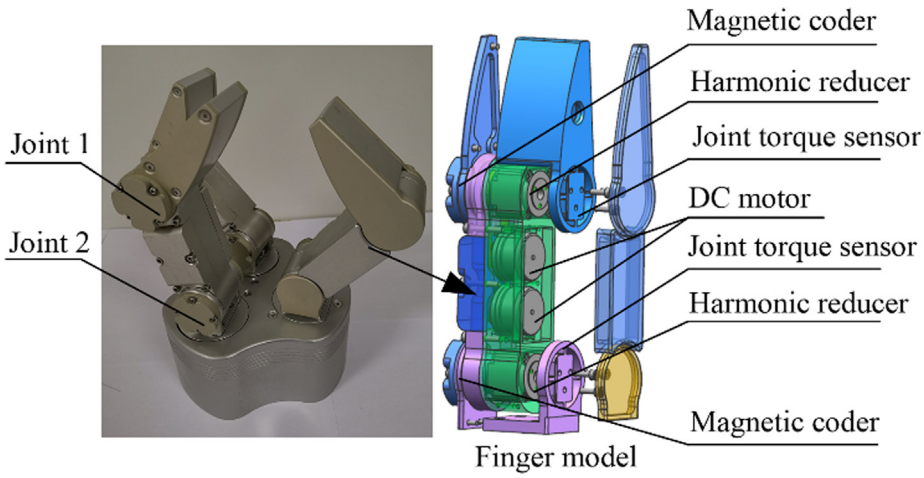

Fig. 1. Three-fingered dexterous hand model.

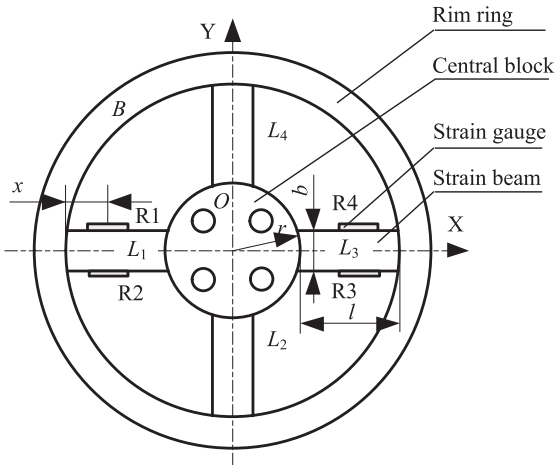

Fig. 2. Schematic diagram of the strain gauge elastomer.

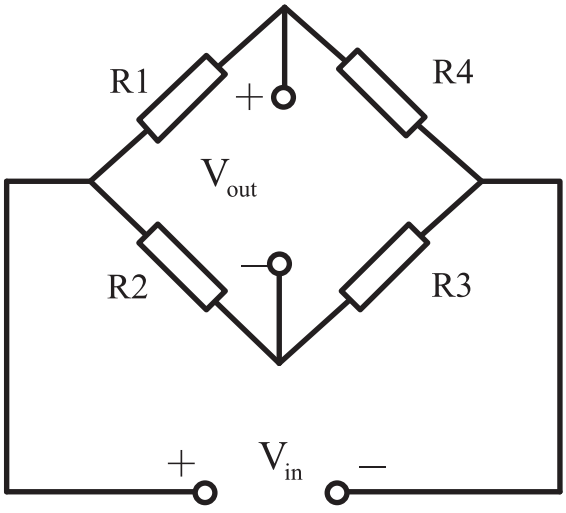

Fig. 3. Full-bridge circuit diagram.

In an ideal sensor, the four strain gauges have the same resistance and symmetrical attachment positions. Therefore, $R_1 = R_2 = R_3 = R_4 = R$ and $\Delta R_1 = \Delta R_2 = \Delta R_3 = \Delta R_4 = \Delta R = RK\varepsilon$, where R is the resistance of the strain gauge, K is the strain constant of the strain gauge and ε is the strain at the attachment position. Eq. (1) can be simplified to:

$$V_{out} = \frac{\Delta R}{R} V_{in} = K\varepsilon V_{in} \tag{2}$$

The sensitivity of a sensor is typically defined as the ratio of the output voltage to the input voltage at full range. The sensitivity G of the finger joint moment sensor can be defined as:

$$G = \frac{V_{out}}{V_{in}} = K\varepsilon_{FS} \tag{3}$$

where ε_{FS} is the micro-strain at the strain gauge attachment position at full range. Eq. (3) shows that the sensitivity of the sensor can be improved by increasing the micro-strain ε_{FS} for a given strain gauge and a given attachment position.

2.3. Problems in miniaturizing the classical torque sensor

Because the sensor elastomer has rotational symmetry, the strain distribution can be determined by analyzing one of its quadrants [29]. The force analysis diagram for the elastomer is shown in Fig. 4. Considering that the strain on the elastic body occurs mainly on the cross beam, rim ring B and central block O are assumed to be rigid bodies, and the deformation of the strain beam is assumed to be within the allowable range.

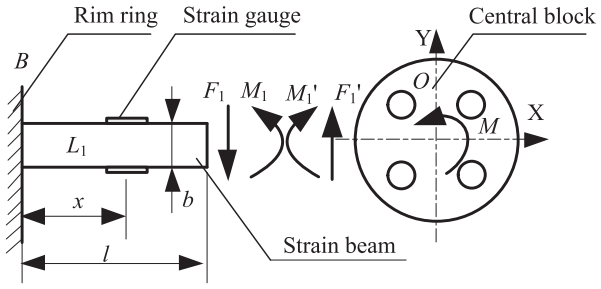

Fig. 4. Force diagram for elastomer in conventional torque sensor.

According to the stress-strain principle and the force-balance principle of a simply-supported beam, the micro-strain ε on the surface of the strain beam can be obtained as:

$$\varepsilon = \frac{Mb}{8EI}\left[\frac{l^2 + 3lr - (3l + 6r)x}{2l^2 + 6lr + 6r^2}\right] \tag{4}$$

where *M* is the moment applied to the elastomer, E is the elastic modulus of the elastomer, *I* is the moment of inertia of the strain beam, and *r*, *l*, *b* and *x* are the geometric parameters shown in Fig. 2.

According to Eq. (4), when *x* is less than $\left(l^2 + 3lr\right)/(3l + 6r)$, the micro-strain on the strain beam is positive; otherwise, it is negative. Choosing a different value of l/r, the transformation between tensile stress and compressive stress on the same side of the strain beam takes place at 1/3to1/2 the length of the beam *l*. Due to the limitations on the space of the finger joint structure, the length of the strain beam is limited by the shape and size of the central block. In practical applications, a chamfer is incorporated to connect the ends of the strain beam and the rim ring or central block, which further reduces the length of the strain beam. It is difficult to improve the sensitivity of a miniature joint torque sensor, even for a small gauge.

2.4. Novel finger joint torque sensor

We developed a miniature finger joint sensor with high sensitivity that is suitable for a dexterous hand. The proposed finger joint torque sensor is shown in Fig. 5. The torque sensor consists of rim ring T, supporting beams L_2 and L_4, strain beams L_1 and L_3, floating beams $L_5 \sim L_8$, connecting block P, and central block O. The supporting beams are parallel to the Y-axis, connected to the rim ring and central block. They increase the Y direction stiffness of the sensor and reduce the interference between the Y direction pressure and the measurement result. The strain beams are parallel to the X-axis, with one end connected to the rim ring and the other end connected to the two floating beams via the connecting block. The floating beams enable flexible deformation between the central block and the connecting block, reducing the restriction of central block on the end of strain beam. The sensor has four floating beams that parallel to the Y-axis. The coordinate origin is at the center of the structure.

The proposed finger joint torque sensor is manufactured from a single block to avoid the measurement delay caused by the clearances between separate components. The proposed torque sensor is symmetrical about the X and Y-axis. According to the force characteristics of the finger joint, the torque sensor bears the pressure in the Y direction and the moment in the Z direction. The pressure

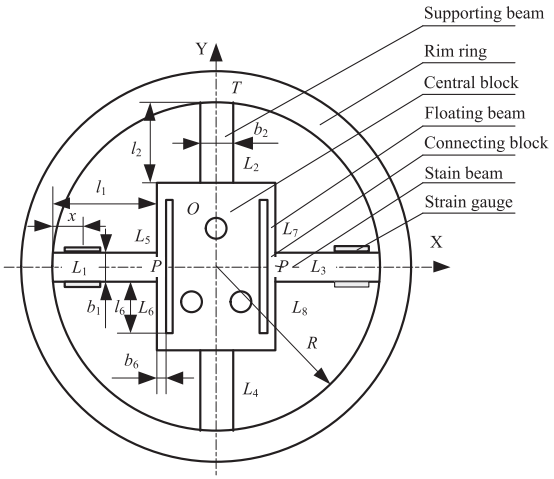

Fig. 5. Model of proposed finger joint torque sensor.

in the Y direction is borne by the supporting beams, and the moment in the Z direction causes a bending deformation in the supporting beam and the strain beam. The moment in the Z direction is measured by strain gauges attached to the strain beam.

A force analysis of the proposed finger joint torque sensor was carried out assuming that rim ring T and central block O are rigid bodies and that only the strain beam and the supporting beam are subjected to elastic deformation. Because the improved elastomer is symmetrical about the X and Y axes, only 1/2 of the elastomer structure needs to be analyzed to obtain the symmetric strain on the whole elastomer. A force analysis diagram of the finger joint torque sensor is shown in Fig. 6.

According to the force analysis of the strain beam L_1, the supporting beam L_2 and the floating beam L_5, the displacement at the end of the beam L_1 ω_1 and the deformed angle at the end of the beam L_1 θ_1 can be obtained as:

$$\begin{cases} \theta_1 = \frac{2M_1l_1 - F_1l_1^2}{2EI_1} \\ \omega_1 = \frac{3M_1l_1^2 - 2F_1l_1^3}{6EI_1} \end{cases} \tag{5}$$

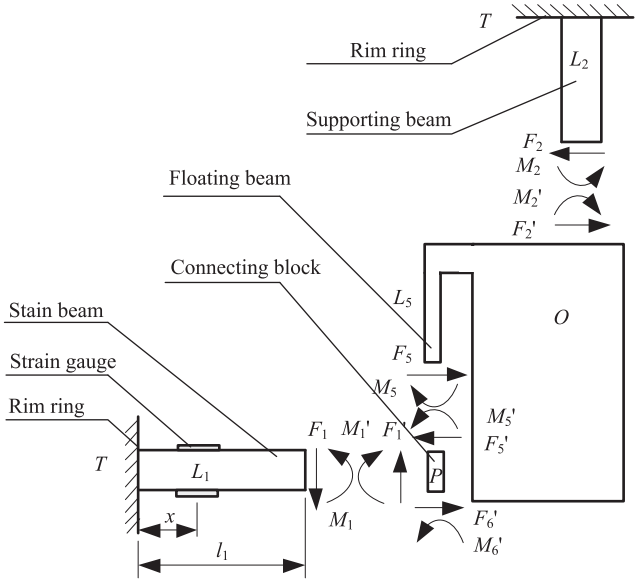

Fig. 6. Force analysis diagram of proposed finger joint torque sensor.

The displacement at the end of the beam L_2 ω_2 and the deformed angle at the end of the beam L_2 θ_2 can be written as:

$$\begin{cases} \theta_2 = \frac{2M_2l_2 - F_2l_2^2}{2EI_2} \\ \omega_2 = \frac{3M_2l_2^2 - 2F_2l_2^3}{6EI_2} \end{cases} \tag{6}$$

The displacement at the end of the beam L_5 ω_5 and the deformed angle at the end of the beam L_5 θ_5 can be written as:

$$\begin{cases} \theta_5 = \frac{2M_5l_5 - F_5l_5^2}{2EI_5} + \theta_2 \\ \omega_5 = \frac{3M_5l_5^2 - 2F_5l_5^3}{6EI_5} + \theta_2 l_5 \end{cases} \tag{7}$$

where F_1, F_2 and $F_5$are the force applied to the strain beam L_1, the supporting beam L_2 and the floating beam L_5, M_1, M_2 and $M_5$are the moment applied to the strain beam L_1, the supporting beam L_2 and the floating beam L_5, I_1, I_2 and I_5 are the moments of inertia of strain beam L_1, supporting beam L_2 and floating beam L_5, respectively. l_1, l_2 and l_5 are the geometric parameters shown in Fig. 5.

According the force-balance principle of the central block and the connecting block, we obtain

$$F_1(R - l_1) + M_1 + F_2(R - l_2) + M_2 = \frac{M}{2} \tag{8}$$

$$M_1 + F_1\frac{b_5}{2} = 2F_5\frac{b_1}{2} + 2M_5 \tag{9}$$

where M is the moment applied to the elastomer, b_1, b_5 and R are the geometric parameters shown in Fig. 5.

As we assume that the connecting block and the central block are rigid bodies, the relationship of deformed angles can be expressed as

$$\begin{cases} -\omega_1 = (R - l_1)\theta_2 - \frac{F_1l_5}{2EA_5} \\ \theta_1 = \theta_5 \\ \omega_2 = -\theta_2(R - l_2) \\ \omega_5 = -\theta_5\frac{b_1}{2} \end{cases} \tag{10}$$

where A_5 is the cross-sectional area of the floating beam.

According Eqs. (5–10), F_1 and M_1 can be respectively expressed as:

$$F_1 = \frac{\frac{3}{2}Kl_1^2l_2^3I_2A_5M}{\left[2l_1^3I_2A_5 + 3l_1^2I_2A_5(R - l_1) + 3I_1I_2l_5\right]\left[2P\left(l_2^2 - 3Rl_2 + 3R^2\right) + Kl_2^3\right]} \tag{11}$$

$$M_1 = \frac{Kl_2^3(l_1^3I_2A_5 - \frac{3}{2}I_1I_2l_5)M}{\left[2l_1^3I_2A_5 + 3l_1^2I_2A_5(R - l_1) + 3I_1I_2l_5\right]\left[2P(l_2^2 - 3Rl_2 + 3R^2) + Kl_2^3\right]} \tag{12}$$

where

$$P = \frac{2l_1^2I_1I_2^2A_5(l_1 + \frac{3}{4}b_5)l_3^5 + 3I_1^2I_2^2I_5l_3^5}{3b_1^2 + 4l_5^2 + 6l_5b_1} - (l_1^4I_2A_5 + 6I_1I_2l_1l_5)I_2I_5 \tag{13}$$

$$K = \frac{I_1I_5\left[3l_1^2I_2A_5R + 3I_1I_2l_5\right]\left(2l_5^2 + 3l_5b_1\right)}{3b_1 + 4l_5^2 + 6l_5b_1} \tag{14}$$

The surface strain on strain beam L_1 can be calculated as:

$$\varepsilon = \frac{b_1}{2EI_1}[F_1(l_1 - x) - M_1] = \frac{Kl_2^3I_2b_1\left[l_1^2A_5(l_1 - 3x) + 3I_1l_5\right]M}{4EI_1\left[2l_1^3I_2A_5 + 3l_1^2I_2A_5(R - l_1) + 3I_1I_2l_5\right]\left[2P(l_2^2 - 3Rl_2 + 3R^2) + Kl_2^3\right]} \tag{15}$$

where x is the distance from the strain attachment position to the rim ring, and b_1 is the width of strain beams.

According to Eq. (15), when $x < \left(l_1^3 A_5 - 3I_1 l_5\right)/3l_1^2 A_5$, the micro-strain ε is a positive value. We can ensure that the strain gauge attachment position has the same strain sign by designing the parameters of the strain beam and floating beam. Eq. (15) also indicates that x and the elastic modulus of the elastomer E are negative for the strain value. because the parameters of the elastomer have a complex relationship with strain value, a parameter optimization method is used to maximize the sensitivity of the torque sensor.

3. Design optimization

3.1. Optimization method

Researchers usually choose alloy steels or aluminum alloys to manufacture the elastomer of torque sensors, because they have a good linearity under the yield limit and isotropy property. According to the design requirements of the dexterous hand, the maximum range of the sensor is ± 2 N·m. We expected to find a material with low elastic modulus, high yield limit, good corrosion resistance and easy to machine. After evaluating several proposals, the torque sensor was manufactured from 7075-T6 aluminum alloy, whose material characteristics are shown in Table 1.

Because the strain beam was very short, a small strain gauge was selected to increase the average micro-strain at the attachment point of the strain gauge. The parameters of the strain gauge are shown in Table 2. To maximize the sensitivity of the sensor in a limited space and ensure that the maximum stress on the sensor remains below the allowable stress of the material, it is necessary to optimize the parameters that affect the sensitivity of the elastomer. Eight parameters affect sensitivity: height h_1, length l_1 and width b_1 of the strain beam, width b_3 and length l_3 of the floating beam, and width b_2, length l_2 and height h_2 of the supporting beam. Because there are many interdependent parameters, RSM was used to optimize the design of the joint torque sensor.

In RSM, appropriate test points for experiments are selected, and a mathematical model is developed for the optimization problem [30]. Then, the parameters corresponding to the optimal results are obtained by finding the optimal solutions to the derived expressions. A flowchart of the optimization process for the proposed sensor is shown in Fig. 7. The key stage is the design of experiments (DOE), which determines the efficiency of the tests and the accuracy of the prediction model equation [31]. There are many methods for designing the test points, including central composite design (CCD), Box-Behnken design, and orthogonal array design. The Box-Behnken method was chosen because it avoids the appearance of extreme points, which can lead to failure or instability of the test results and is highly suitable for mechanical size optimization [30,32]. The ranges for parameters required for the joint torque sensor to remain within the overall size limitations are shown in Table 3. For the three-level eight-factorial Box-Behnken experimental design, a total of 120 experiments were designed using the software Design-Expert. Each group was modeled and analyzed using finite element method (FEM) software. The micro-strain and maximum stress were recorded.

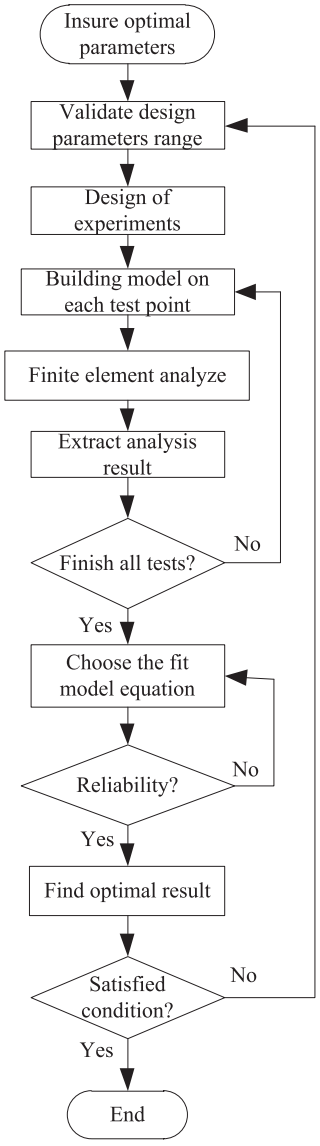

Fig. 7. Flowchart of optimization process.

Table 1
Characteristics of 7075-T6 aluminum alloy.

Property	Density (g/cm^3)	Young's Modulus (MPa)	Poisson's Ratio	Yield Strength Sy (MPa)	Ultimate strength Su (MPa)
value	2.80	71.7	0.33	460	530

Table 2
Strain gauge specifications.

parameters	substrate dimensions	gauge dimensions	Gauge Resistance	gauge factor
contents	3 mm × 2 mm	1 mm × 1 mm	120 ± 2 Ω	2.0

Table 3
Parameter ranges for proposed joint moment sensor.

variable	h1	h2	l1	l2	l3	b1	b2	b3	ε_{FS}	σ_{FS}
range	3 ~ 4.2	2 ~ 4.2	5.2 ~ 6.2	3 ~ 5.6	3 ~ 5.6	1.4 ~ 4	1.6 ~ 5	0.5 ~ 1.3	Maximum	≤101Mpa
Optimal Results	3.00	3.16	6.00	3.00	4.97	1.40	1.68	0.50	1282.47	101

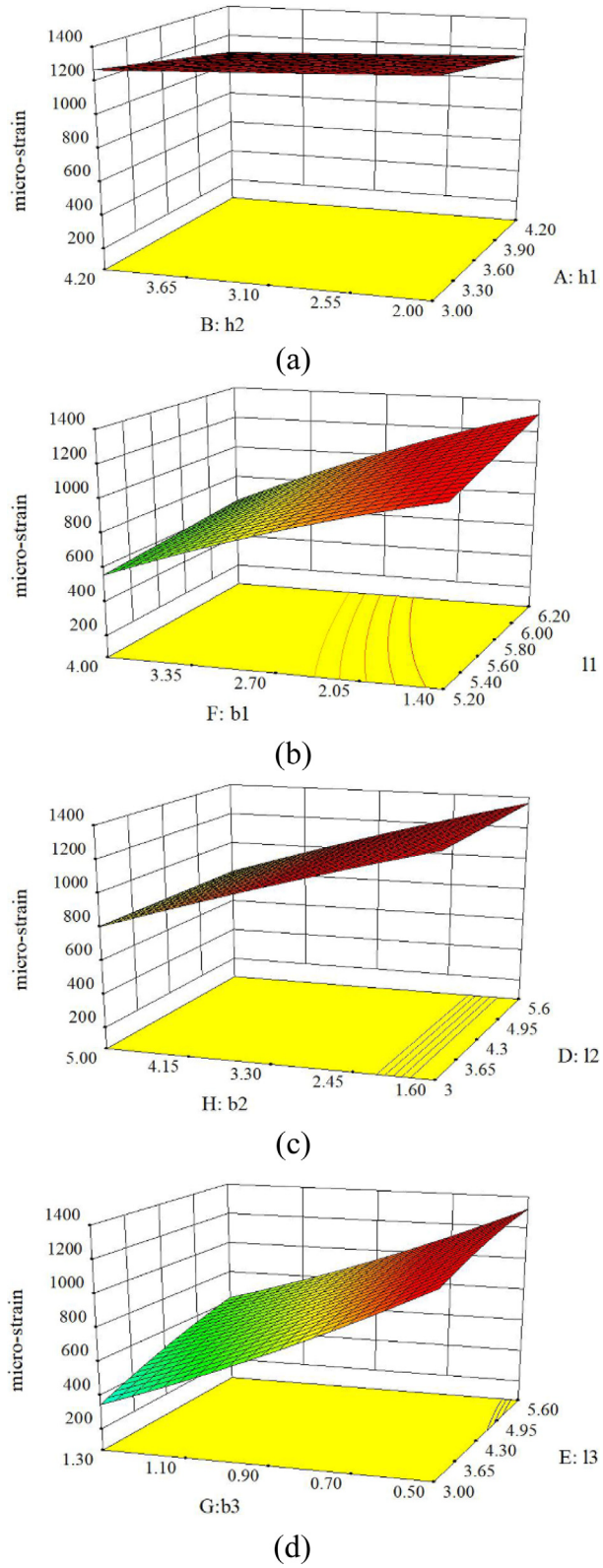

Fig. 8. Response surface for micro-strain vs independent variables.

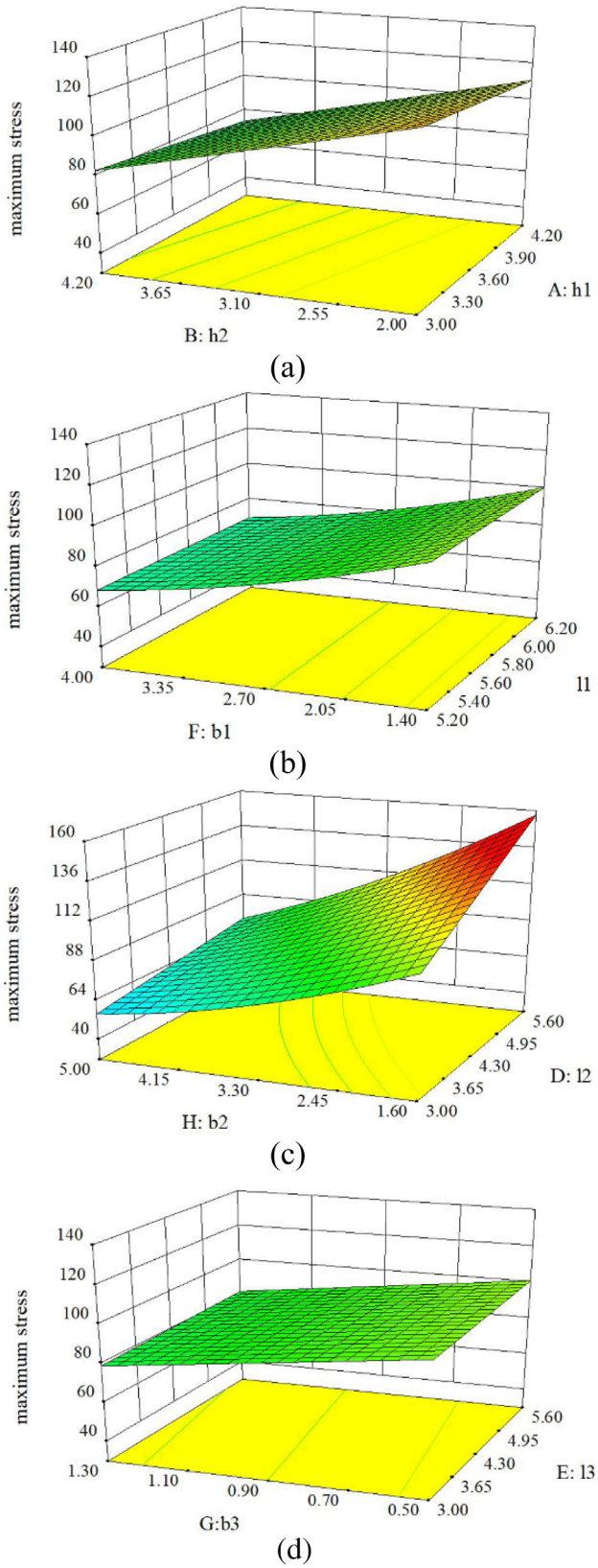

Fig. 9. Response surface for maximum stress vs independent variables.

Table 4
Values and residuals form ANOVA.

	p values	R^2	Adjusted R^2	Predicted R^2	Adequate precision
micro-strain	< 0.0001	0.95	0.94	0.91	41.69
maximum stress	< 0.0001	0.94	0.92	0.89	31.99

3.2. Optimized results

A comparison of linear, two-factor interaction, quadratic, and cubic equations [33], showed that the quadratic equation best approximated the relationship between the independent parameters and the response surface. The regression coefficient of the quadratic equation, with insignificant terms neglected, was obtained using least squares. The micro-strain ε_{FS} and maximum stress σ_{FS} are respectively expressed as:

$$\begin{aligned}\varepsilon_{FS} = {} & 1042.89 - 188.64h_1 - 58.21h_2 + 280.95l_1 + 198.47l_3 \\ & + 90.18b_1 - 3017.97b_3 + 32.15b_2 + 20.31h_1b_2 \\ & + 49.32h_2b_3 - 44.67l_1b_1 + 110.96l_1b_3 - 38.41l_1b_2 \\ & - 15.57l_3b_1 + 59.14l_3b_3 - 14.41l_3b_2 + 209.57b_1b_3 \\ & + 19.93b_1b_2 + 143.47b_3b_2 - 13.49l_3^2 - 24.01b_1^2 \\ & + 239.85b_3^2 - 5.98b_2^2 \end{aligned} \quad (16)$$

$$\begin{aligned}\sigma_{FS} = {} & 686.35 - 108.36h_1 - 23h_2 - 71.01l_1 + 11.47l_2 \\ & - 45.13l_3 - 29.11b_1 - 54.22b_3 - 7.89b_2 + 13.08h_1l_1 \\ & + 3.47h_1l_3 + 3.52h_1b_1 - 2.35h_2l_2 - 1.4h_2l_3 \\ & + 10.05h_2b_3 + 4.88h_2b_2 + 3.93l_1l_2 + 5.57l_1l_3 - 4l_1b_2 \\ & + 1.44l_2l_3 - 2.75l_2b_1 - 5.61l_2b_3 - 4.33l_2b_2 \\ & - 1.21l_3b_2 + 1.59b_1b_2 + 8.98b_3b_2 + 2.25b_1^2 + 2.27b_2^2 \end{aligned} \quad (17)$$

The relationships between the independent variables and the micro-strain and maximum stress are shown in Figs. 8 and 9, respectively. The sensitivities of the input parameters are shown in Fig. 10. As shown, the micro-strain is very sensitive to b_3, b_1, and b_2 and the maximum stress is sensitive to b_1. The input parameters l_1 and l_3 have a positive effect on ε_{FS} and σ_{FS}, whereas the parameters h_1, h_2, b_1, b_2, and b_3 have a negative effect. The input parameter b_1 has almost the same effect on ε_{FS} and σ_{FS}, whereas parameter l_2 has a positive effect on σ_{FS}, but a negligible effect on ε_{FS}.

Analysis of variance (ANOVA) was conducted for the approximate models of ε_{FS} and σ_{FS}. The results are shown in Table 4. For both models, p less than 0.0001, $R^2 > 0.9$, and the adjusted values are close to the predicted values. The precision is above 4, which is adequate. these results show that the mathematical models for micro-strain and maximum stress established based on Eqs (16) and (17) are stable and reliable. These equations can thus be used to optimize the models.

To ensure that the elastomer is not destroyed, the condition $\sigma_{FS} \leqslant \sigma_s/S$ must be satisfied, where σ_s is the material yield strength shown in Table 1 and S is the safety factor. Because the sensor is affected by forces other than the torque in the direction of measurement, a safety factor S was set to 4.5. The optimization objective that will maximize micro-strain ε_{FS} can be expressed as $\sigma_{FS} \leqslant 101$Mpa. The optimal parameters shown in Table 3 were obtained using a search algorithm. Table 3 shows that the micro-strain was 1282.47 and the maximum stress was 99.54 MPa after optimization. The optimization model is shown in Fig. 11.

4. Strain analysis

MSC/Patran was used to mesh the optimized model. The finger joint torque sensor using conditions allowed the degrees of freedom of the node at the bottom of the rim ring to be set to zero.

Torque was applied via the three screw holes in the central block. Since the sensor works under the yield limit, it is assumed that the deformation of the elastomer is linear. The finite element mesh model is shown in Fig. 12. The corresponding material properties were input into the finite element model and the stress was calculated with MSC/Nastran. The strain nephogram of the sensor in the direction of attachment of the strain gauge is shown in Fig. 13, which shows that the strain gauge had the largest strain near the fixed ring, consistent with the theoretical analysis. Fig. 14 shows Strain distribution on surface of the strain beam. Because of the machined chamfer the strain gauge was attached at a position 0.5 mm away from the fixed ring. Considering the substrate dimensions were larger than the gauge dimensions the average strain on the strain beam at a distance of 1–2 mm from the rim ring was used to calculate the strain on the strain gauge.

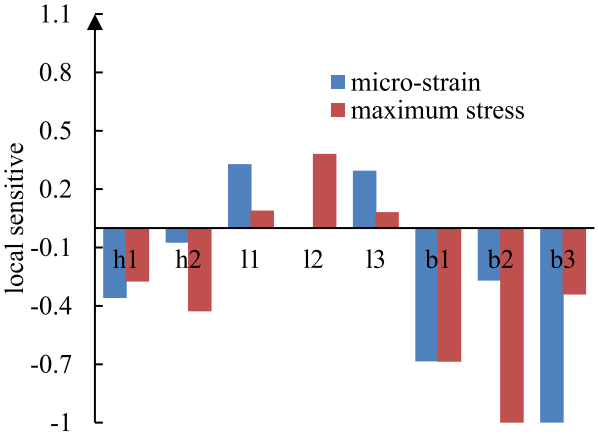

Fig. 10. Sensitivities of input parameters.

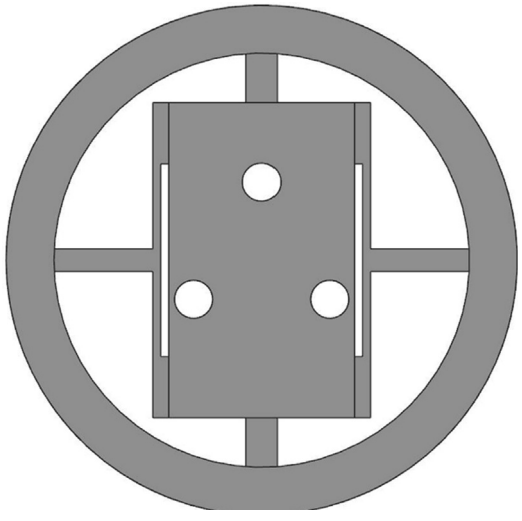

Fig. 11. Optimized joint torque sensor model.

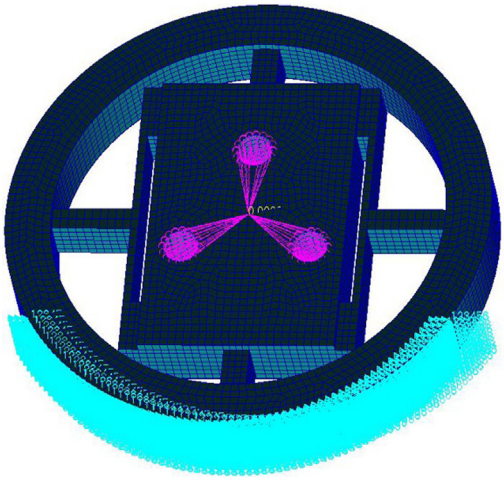

Fig. 12. FEM mesh used for the finger joint torque sensor.

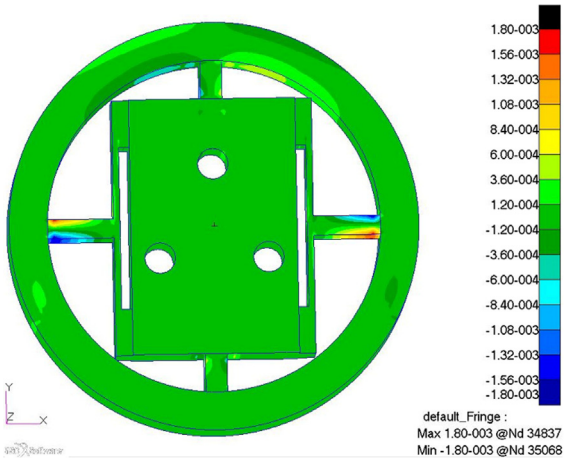

Fig. 13. Strain nephogram in direction of beam strain.

The average value of the micro-strain at the attachment position was 1288 and the maximum stress was 100 MPa, these values are close to the results for the response surface. This verifies that the optimized parameters can be used to manufacture the proposed finger joint torque sensor.

5. Calibration test

5.1. Calibration method

A prototype of the torque sensor was fabricated and the strain gauges were attached in accordance with the FEM results. The finger joint torque sensor shown in Fig. 15 has a torque range of ± 2 N·m, and dimensions of Φ31 mm × 4.2 mm. To obtain the performance of the designed finger joint torque sensor accurately, it was necessary to calibrate the torque sensor. The calibration platform is shown in Fig. 16. The torque was applied alone based on the pulley-weight principle. The signal output by the strain gauge was amplified by a strainmeter and sent to a computer via a data acquisition board.

5.2. Calibration results

Five loading and unloading tests were carried out in the range of ± 2 N·m. Ten sets of data were obtained for each moment point. A comparison of these 10 sets of data at each loading point, indi-

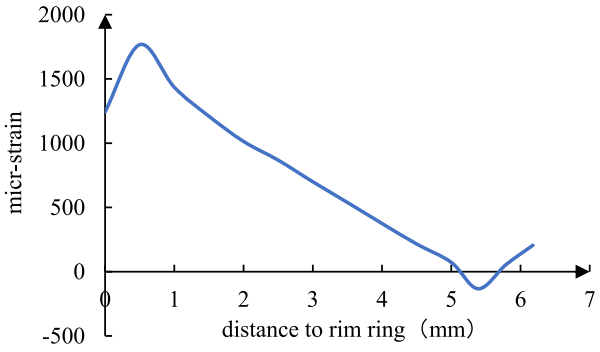

Fig. 14. Strain distribution on surface of the strain beam.

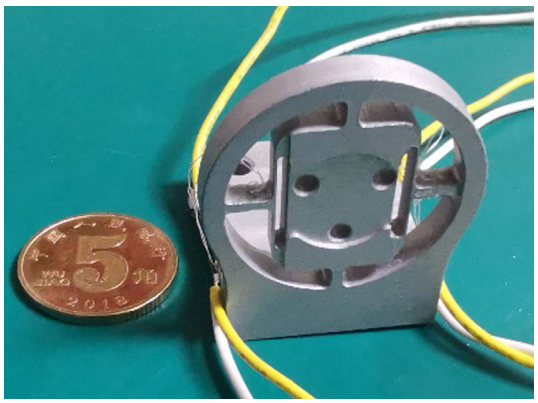

Fig. 15. Prototype finger joint torque sensor.

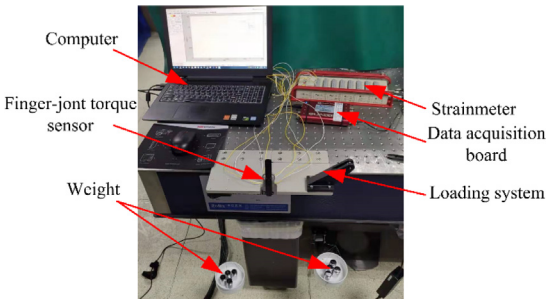

Fig. 16. Calibration platform.

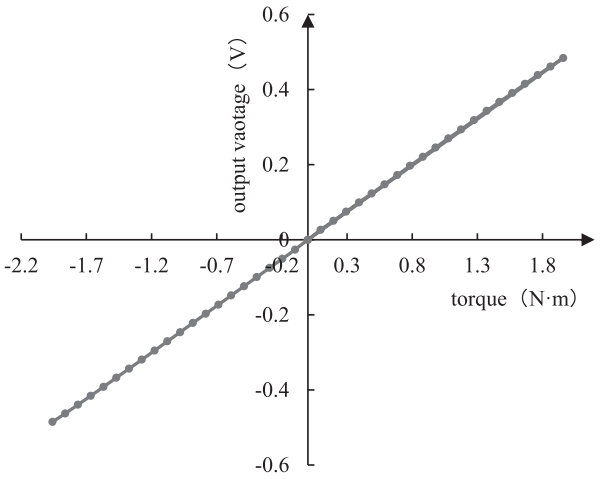

Fig. 17. Loading curve for finger joint torque sensor.

Table 5
Sensor sensitivity.

Sensor sensitivity (mV/V)		
FEM	Exp	Error (%)
2.48	2.44	1.64

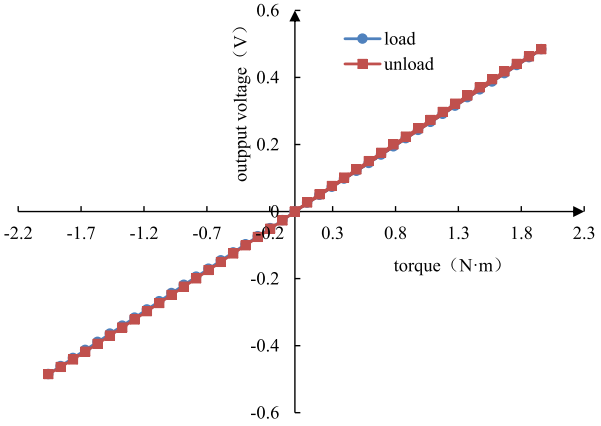

Fig. 18. Hysteresis curve of proposed sensor.

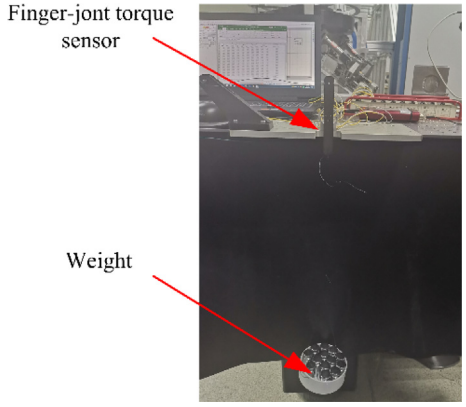

Fig. 19. Load in the direction of the supporting beam.

cated a sensor error of 1.84% full scale (F.S.). The least squares method was used to obtain a linear fit for the loading curve for the finger joint torque sensor. The results are shown in Fig. 17. From the loading curve and the distribution of points, the linearity error of the finger joint torque sensor was calculated to be 0.62% F.S. The mean residual error distribution was 2.4×10^{-6} and the standard deviation of the normal distribution was 0.0017, which indicate that the sensor has good linearity and repeatability.

Table 5 compares the sensitivity calculated using finite element analysis with that measured by experiment. The error between the analysis results and the experimental values is 1.64%. The main reason for this error is that the actual attachment positions and directions of the strain gauges were different from the theoretical positions and directions, which resulted in the strain measured by the strain gauge being less than the analytical value. The sensitivity of the sensor can be improved by further improving the positioning accuracy of the strain gauges.

The average values were calculated for five points in the loading process and five points in the unloading process. The hysteresis curve of the sensor is shown in Fig. 18. As shown, the loading curve coincides with the unloading curve. The hysteresis error for the sensor of less than 1.48% F.S.

The finger joint moment sensor mainly bears the measurement moment and the force in the direction of the supporting beam. To determine whether there was any interference from the force in the direction of the supporting beam on the measurement results, the test platform was improved and a tension force was applied in the direction of the supporting beam, as shown in Fig. 19. For the test, 21 loading points were evenly distributed in the range of 0–20 N, but the measured output of the torque sensor remained unchanged, indicating that the force in the direction of the supporting beam did not interfere with the measurement results.

Table 6 compares the finger joint torque sensor we designed with other torque or force/torque sensors, which shows that the sensitivity of the torque sensor we designed is higher than most of other sensors except literature [11]. However, the diameter of the sensor introduced by literature [11] is Φ150, and the structure of 4-bar linkage shape is difficult to achieve the miniaturization. Literatures [14], [21], [22] and [27] have a smaller size, but there is no introduce about the sensitivity. Moreover, hysteresis of literatures [22] and [27] is too high to realize the precise measurement. In summary, the torque sensor introduced by this paper has an advantage in sensitivity, under the consideration of volume. At the same time, torque range, linearity, and Hysteresis can fit for the torque measurement of finger joints very well.

6. Conclusion

This study proposed a joint torque sensor with floating beams and supporting beams. The size of the sensor is Φ34mm × 4.2 m m, which can meet the space requirement of finger joints. The structural parameters of the sensor were optimized using RSM to maximize sensor sensitivity. The optimized model was analyzed by FEM, and a prototype sensor was fabricated and calibrated. The results show that the sensitivity of the sensor was 2.44 mV/V which is higher than most of the torque sensors, the linearity

Table 6
Compared with other torque or force/torque sensors.

Work	Axes	Technology	Torque range (N·m)	Size (mm)	Sensitivity (mV/V)	Linearity (%F.S.)	Hysteresis (%F.S.)
Liang Q et al. [14]	4	strain gauges	±1	Φ30 × 35	–	0.2	–
Mouri T et al. [27]	1	strain gauges	±0.4	Φ13 × 1.5	–	2.3	9.3
Yuan C et al. [12]	6	strain gauges	±10	Φ50 × 12	2.26	0.62	0.73
Sun Y et al. [10]	6	strain gauges	±98	Φ224 × 32.4	1.55	0.37	0.28
Lee D H et al. [21]	6	capacitive	±1	Φ25 × 19	–	1.07	0.93
Pérez R U et al. [9]	1	strain gauges	±1	Φ65 × 6	2.01	1.27	3.54
Noh Y et al. [22]	3	optoelectronic	±0.09	Φ24 × 12	--	–	22.6
Kashiri N et al. [16]	1	strain gauges	±150	Φ63	1.26	--	–
Zhang H X et al. [11]	1	strain gauges	±40	Φ150	2.75	1.5	–
Khan H et al. [17]	1	strain gauges	±60	Φ40 × 15	1.7	0.23	--
Ours	1	strain gauges	±2	Φ34 × 4.2	2.44	0.62	1.48

error was 0.62% F.S., hysteresis error less than 1.48%F.S. and the repeatability error less than 1.84%F.S.. We verified that the force in the direction of the supporting beam did not interfere with the torque measurement. The sensor performed exceptionally well in testing and can be used for moment feedback in the finger joint of a manipulator. The analysis and optimization methods adopted in this paper can be applied to other sizes and types of torque sensors.

In the future, semiconductor strain gauges will be tested on the torque sensor of finger joint, as they have a smaller size and higher gauge factor, which are beneficial to improve the measurement sensitivity further. At the same time, the signal process circuit will be designed to enhance the signal-to-noise ratio.

Declaration of Competing Interest

The authors declare that they have no known competing financial interests or personal relationships that could have appeared to influence the work reported in this paper.

Acknowledgment

This work was supported by the National Natural Science Foundation of China [grant number 11672290].

References

[1] H. Liu, K. Wu, P. Meusel, et al., Multisensory five-finger dexterous hand: The DLR/HIT Hand II[C]//2008 IEEE/RSJ international conference on intelligent robots and systems, IEEE (2008) 3692–3697.
[2] J. Butterfass, M. Grebenstein, H. Liu, DLR-Hand II: Next generation of a dextrous robot hand[C]//proceedings 2001 ICRA. IEEE International Conference on Robotics and Automation (Cat. No. 01CH37164), IEEE 1 (2001) 109–114.
[3] A. Barrea, D. Cordova Bulens, P. Lefevre, et al., Simple and reliable method to estimate the fingertip static coefficient of friction in precision grip[J], IEEE Trans. Haptics (2016), 1 1.
[4] D.L. Jindrich, A.D. Balakrishnan, J.T. Dennerlein, Finger joint impedance during tapping on a computer keyswitch[J], J. Biomech. 37 (10) (2004) 1589–1596.
[5] Y.F. Ki, S.K. Tso, Q. Meng, Grasping force measurement for dynamic grasp stability assessment[J], IEEE Trans. Instrum. Meas. 47 (5) (1998) 1294–1299.
[6] P. Martin, C. Maxime, S. Freek, et al., Fusing joint measurements and visual features for in-hand object pose estimation[J], IEEE Rob. Autom. Lett. (2018), 1 1.
[7] B.M. Finio, K.C. Galloway, R.J. Wood, 2011. An ultra-high precision, high bandwidth torque sensor for micro robotics applications[C]// 2011 IEEE/RSJ International Conference on Intelligent Robots and Systems, IROS 2011, San Francisco, CA, USA, September 25-30, 2011. IEEE.
[8] Y. Yu, T. Ishitsuka, S. Tsujio, 2003. Torque sensing of finger joint using strain-deformation expansion mechanism.[C]// IEEE International Conference on Robotics. IEEE.
[9] R.U. Pérez, S.R. Gutiérrez, R.S. Zotovic, et al., Design and Manufacturing of an ultra-low-cost custom torque sensor for robotics[J], Sensors 18 (6) (2018) 1786–1804.
[10] Y. Sun, Y. Liu, T. Zou, et al., Design and optimization of a novel six-axis force/torque sensor for space robot[J], Measurement 65 (2015) 135–148.
[11] H.X. Zhang, Y.J. Ryoo, K.S. Byun, Development of torque sensor with high sensitivity for joint of robot manipulator using 4-bar linkage shape[J], Sensors 16 (7) (2016) 991.
[12] C. Yuan, L.P. Luo, Q. Yuan, et al., Development and evaluation of a compact 6-axis force/moment sensor with a serial structure for the humanoid robot foot [J], Measurement 70 (2015) 110–122.
[13] Q. Liang, D. Zhang, Q. Song, et al., Design and fabrication of a six-dimensional wrist force/torque sensor based on E-type membranes compared to cross beams[J], Measurement 43 (10) (2010) 1702–1719.
[14] Q. Liang, D. Zhang, Q. Song, et al., A potential 4-D fingertip force sensor for an underwater robot manipulator[J], IEEE J. Oceanic Eng. 35 (3) (2010) 574–583.
[15] M.K. Kang, S. Lee, J.H. Kim, Shape optimization of a mechanically decoupled six-axis force/torque sensor[J], Sens. Actuators, A 209 (2014) 41–51.
[16] N. Kashiri, J. Malzahn, N.G. Tsagarakis, On the sensor design of torque controlled actuators: A comparison study of strain gauge and encoder-based principles[J], IEEE Rob. Autom. Lett. 2 (2) (2017) 1186–1194.
[17] H. Khan, M. D'Imperio, F. Cannella, et al., Towards scalable strain gauge-based joint torque sensors[J], Sensors 17 (8) (2017) 1905.
[18] ATI Industrial Automation F/T Sensor: Nano 17 https://www.ati-ia.com/Library/Software/FTDigitaldownload/getcalfiles.aspx.
[19] C. Melchiorri, L. Moriello, G. Palli et al., 2014. A new force/torque sensor for robotic applications based on optoelectronic components[C]// IEEE International Conference on Robotics & Automation. IEEE.
[20] M. Kaneko, K. Yokoi, K. Tanie, On a new torque sensor for tendon drive fingers [J], IEEE Trans. Rob. Autom. 6 (4) (1990) 501–507.
[21] D.H. Lee, U. Kim, H. Jung, et al., A capacitive-type novel six-axis force/torque sensor for robotic applications[J], IEEE Sens. J. 16 (8) (2015) 2290–2299.
[22] Y. Noh, J. Bimbo, S. Sareh, et al., Multi-axis force/torque sensor based on simply-supported beam and optoelectronics[J], Sensors 16 (11) (2016) 1936.
[23] K. Jung, S. Shin, K. Lee et al., 2012. Evaluation of fingertip F/T sensor for dexterous manipulation[C]// 2011 8th International Conference on Ubiquitous Robots and Ambient Intelligence (URAI). IEEE.
[24] Y. Hwang, Y. Minami, M. Ishikawa, Virtual torque sensor for low-cost RC servo motors based on dynamic system identification utilizing parametric constraints[J], Sensors 18 (11) (2018) 3856.
[25] T.K. Kim, D.Y. Kim, D.H. Cha et al., 2013. Development of joint torque sensor and calibration method for robot finger[C]//2013 10th International Conference on Ubiquitous Robots and Ambient Intelligence (URAI). IEEE, pp. 161–162.
[26] B.J. Jung, B. Kim, H.R. Choi, et al., Joint torque sensor embedded in harmonic drive using order tracking method for robotic application[J], IEEE/ASME Trans. Mechatron. (2017), 1 1.
[27] T. Mouri H. Kawasaki K. Koketsu, 2011. Compact torque sensor for a robot hand[C]// International Conference on Ubiquitous Robots & Ambient Intelligence. IEEE.
[28] D.H. Kim B.S. Kim J.H. Hwang et al., 2011. The new 2 DOF frame torque sensor for the Metacarpophalangeal joint in robotic hand[C]// International Conference on Ubiquitous Robots & Ambient Intelligence. IEEE.
[29] G.S. Kim, D.I. Kang, S.H. Rhee, Design and fabrication of a six-component force/moment sensor[J], Sens. Actuators, A (Phys.) 77 (3) (1999) 209–220.
[30] D. Ba, Smail H. Boyac, Modeling and optimization I: usability of response surface methodology[J], J. Food Eng. 78 (3) (2007) 836–845.
[31] M.A. Bezerra, R.E. Santelli, E.P. Oliveira, et al., Response surface methodology (RSM) as a tool for optimization in analytical chemistry[J], Atlanta 76 (5) (2008).
[32] S.L.C. Ferreira, R.E. Bruns, H.S. Ferreira, et al., Box-Behnken design: an alternative for the optimization of analytical methods[J], Anal. Chim. Acta 597 (2) (2007) 179–186.
[33] J.T. Li, Z.J. Liu, M.A. Jabbar, et al., Design optimization for cogging torque minimization using response surface methodology[J], IEEE Trans. Magn. 40 (2) (2004) 1176–1179.